MIT Open Access Articles

Silicon photonics devices for integrated analog signal processing and sampling

Massachusetts Institute of Technology

Review article

Steven Spector* and Cheryl Sorace-Agaskar

Silicon photonics devices for integrated analog signal processing and sampling

Abstract: Silicon photonics offers the possibility of a reduction in size weight and power for many optical systems, and could open up the ability to build optical systems with complexities that would otherwise be impossible to achieve. Silicon photonics is an emerging technology that has already been inserted into commercial communication products. This technology has also been applied to analog signal processing applications. MIT Lincoln Laboratory in collaboration with groups at MIT has developed a toolkit of silicon photonic devices with a focus on the needs of analog systems. This toolkit includes low-loss waveguides, a high-speed modulator, ring resonator based filter bank, and all-silicon photodiodes. The components are integrated together for a hybrid photonic and electronic analog-to-digital converter. The development and performance of these devices will be discussed. Additionally, the linear performance of these devices, which is important for analog systems, is also investigated.

Keywords: silicon photonics; silicon modulator; silicon photodetector; ring resonator filters.

*Corresponding author: Steven Spector, Lincoln Laboratory, Massachusetts Institute of Technology, 244 Wood Street, Lexington, MA 02420, USA, e-mail: spector@ll.mit.edu
Cheryl Sorace-Agaskar: Research Laboratory of Electronics, Massachusetts Institute of Technology, 77 Massachusetts Avenue, Cambridge, MA 02139, USA

1 Introduction

In just over the last decade, the state-of-the-art in silicon photonics has quickly developed from a few poorly performing passive devices to complete toolset of high performance optical components. Recently, there was a demonstration of a 4 channel WDM communication implemented completely using silicon photonics [1], and at least two organizations [2, 3] now offer complete silicon photonics foundry services.

In this review paper, we review the development of silicon photonics at MIT Lincoln Laboratory in collaboration with MIT. In these efforts silicon photonics has been developed in parallel with other research groups, and many of the technologies are similar. The components developed at Lincoln Laboratory and MIT include low-loss waveguides, filters, modulators, and the detectors. One technology that is somewhat unique is the use of all-silicon photo-detectors, instead of the more common germanium based detectors. The target application for much of the work in silicon photonics is digital communication, but there are many possible analog applications for silicon photonics such as optical sampling for an analog-to-digital converter (ADC) [4], RF waveform generation [5], and RF down-conversion [6]. The components fabricated at Lincoln Laboratory were developed for the target application of an ADC [4], and this choice guided the specifications for these devices. For example, the modulator needed to be able to simultaneously modulate a number of wavelengths. This necessitated the use of a Mach-Zehnder interferometer for the modulator, instead of a lower power and more compact ring resonator.

Many of the component designs can be shared between analog and digital applications, but analog applications often have more challenging requirements. In particular, analog applications typically require a greater signal to noise ratio (SNR) and lower non-linearity than digital applications. These two requirements are often challenging to simultaneously achieve. A large amount of optical power is necessary for low SNR, however, increasing optical power increases the amount of non-linearity in an optical system. Silicon photonics is particularly susceptible to severe non-linear performance because the light is confined to very compact structures, which increases the mode intensity in the silicon. In addition, resonant devices, such as ring resonator filters, further concentrate the light, further increasing susceptibility to non-linearity.

In this paper we will describe the silicon photonic components that have been developed at Lincoln Laboratory in collaboration with MIT. After the description of the components, the issue of non-linearity and silicon photonics will be discussed. Then, a description of a demonstration of the components being integrated together for a hybrid photonic and electronic ADC is presented.

2 Low-loss waveguides by waveguide widening

Perhaps the most basic device in an integrated photonic circuit is the wire or waveguide used to guide the light around a circuit. The large difference between the refractive index of silicon (n~3.45) and the silicon oxide typically used as a cladding (n~1.45), allows very compact waveguides to be created in silicon. The small size of the waveguide has many benefits. It allows many devices to be fabricated in a small chip area. Small size means lower electrical power is needed by many devices, because less volume needs to be electrically affected to get a similar response. The smaller size also allows the waveguides to be fabricated using CMOS tools and processes which are optimized for similar dimensions. However, such small waveguides have some disadvantages. Fabrication tolerances, to a large degree, scale with the size of the waveguide, therefore smaller waveguides may have much tighter fabrication tolerances. The implications of this will be discussed in the section on filter fabrication.

Another disadvantage of highly confined waveguides is that such waveguides are susceptible to significant optical loss due to light scattering from any imperfections in the waveguide, such as sidewall roughness. The compactness of silicon waveguides does mean that many of the devices are small, and fairly high propagation losses can sometimes be tolerated. However, many devices such as ring resonator filters, still require low optical loss to achieve adequate performance. In some applications long paths are necessary. For example, long paths can be used to create time delays, or long paths are simply needed to route signals long distances across a chip. Scattering from waveguide roughness not only causes optical loss, but some of the light can be scattered into the reverse direction in the waveguide [7]. This reverse propagating light can degrade signals and also degrade filter performance [8].

There are a number of ways to lower the scattering from waveguide roughness, the most obvious being to lower the amount of roughness in waveguide. This can be done by either smoothing the waveguide after etching, or by improving the smoothness of the waveguide when it is etched. Some examples are using oxidation for after etch improvement [9] or resist reflowing to improve the smoothness of the resist mask for the waveguide etch [8]. These methods can modestly improve optical loss, but they change the final dimensions of the waveguide relative to the original lithographic dimensions.

Another method to lower the loss of waveguide is to reduce the effective index contrast of the waveguide. This can done by using a rib structure (i.e., incompletely etching the silicon surrounding the waveguide) [10], or by using a thinner silicon layer [11]. Reducing the index contrast increases the mode size and this can be very effective in lowering optical loss. Losses as low as 2.7 dB/m have been demonstrated in silicon waveguides [10], and, by applying the technique to nitride waveguides, losses as low as 0.045 dB/m can be achieved [12]. Lowering the effective index contrast does have the disadvantage of leading to much larger structures, however. In the silicon nitride example above, the bending radius was limited to >1 cm. Both resist smoothing and using thinner silicon layers have been explored by us as methods to improve filter performance, and will be discussed in the section on filters.

A third method for lowering loss is to widen a waveguide. Widening a waveguide, decreases the mode intensity at the sidewall, significantly decreasing the optical loss. The improvement is considerable, as scattering scales with width, w, as w^{-4} [13]. However, a larger waveguide often supports more than one mode, and multi-mode performance is not desirable for most applications. It is possible to use a multi-mode waveguide in a single-mode fashion if excitation of the unwanted higher modes can be avoided. One way to avoid the excitation of higher order modes is to use a straight waveguide with no defects, and adiabatically couple to such a waveguide from a single-mode waveguide [14]. Inevitably, the wide waveguide will not be perfect, and roughness will cause some coupling to higher order modes. However, light in the higher order modes cannot be supported by a single-mode waveguide and will leak into the cladding if a transition is made back into the single mode waveguide, adiabatically. Once the light has transitioned to a single mode waveguides, the light can be coupled to a tight bend or any other desired structure.

To verify this technique hybrid single-mode/multi-mode SOI waveguides were created with 0.7 mm long, 5 μm wide multimode regions connected adiabatically to two 480×205 nm waveguide single-mode regions at
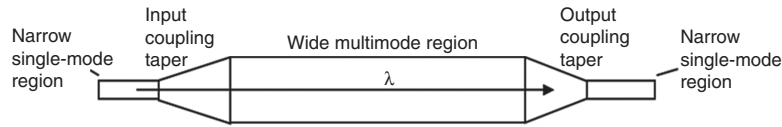
Figure 1 Diagram of wide waveguide with adiabatic tapers to narrow single mode regions.

the beginning and end of the wide region, shown schematically in Figure 1. The adiabatic transitions used linear tapers, 90 µm long. These structures were cleaved through the narrow regions to create a Fabry-Perot resonator between the two facets, and Figure 2A shows the observed transmission fringes. The fringes are fairly regular, and frequency analysis of the fringes indicates only one fringe frequency. This indicates that the combined structure of single mode and multimode waveguides only has one propagation mode. Figure 2B shows the transmission through a simple 480×205 nm waveguide, also cleaved to create Fabry-Perot fringes. Again, only a single fringe frequency is present in the data, however, there is greater noise to the fringes. This noise is believed to be caused by light that is backscattered randomly from the sidewall roughness in the waveguide, creating noisy interference. Comparing the simple single-mode waveguide to the hybrid waveguide, there is much less noise indicating that much less light is being backscattered in the waveguide.

Long propagation paths were also created using this technique by creating 180° bends in narrow waveguides connected to straight wide waveguides. Loss measurements were made at a wavelength of 1540 nm by comparing the transmission through different path lengths using paperclip structures [14]. In these experiments, the propagation loss of a simple single-mode waveguide is 2.7 dB/cm, and the propagation loss of the wide sections alone are 0.4 dB/cm. In a combined structure, with straight wide waveguides that are 1.73 cm long between bends, the net propagation loss is 0.6 dB/cm. This loss can be further lowered

by using oxidation smoothing on the waveguides. For this test, 335 nm of oxide was grown by wet thermal oxidation at 1100°C. Oxidation changes the dimensions of the waveguide, so the initial size of the single-mode waveguide was 800 nm wide and 500 nm thick before oxidation. The final dimensions of the single-mode waveguide are 450×210 nm, however, the wide waveguides regions are 350 nm thick. The propagations losses are 2.8 dB/cm, 0.2 dB/cm, and 0.3 dB/cm, for the narrow, wide, and combined paths, respectively. For reasons unknown, oxidation did not improve the loss for the narrow regions, however the loss in the wide region is much lower with oxidation. It is not clear if this loss reduction is due to smoother profile of the waveguide or due to the fact that the added thickness in the wide regions further expands the mode. It should be pointed out that although the intrinsic material loss of silicon is very low (<0.01 dB/cm for ~10 Ω·cm n-type silicon), damage to the silicon from the etch process also may be impacting the waveguide loss [7].

3 Optical modulator

Optical modulation in silicon is typically achieved using the free-carrier plasma dispersion effect [15], although electro-absorption modulation using the Franz–Keldysh effect in germanium on silicon has also been used [16]. The free-carrier plasma dispersion effect causes a change in the refractive index and absorption of silicon when
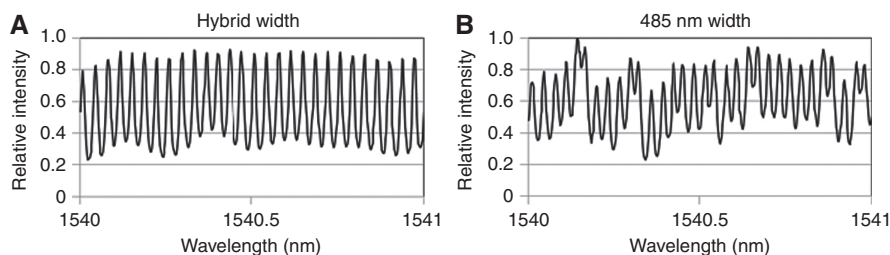

Figure 2 The transmission spectra of 8.3 mm lengths of waveguides. The reflections from cleaved facets of the waveguides produce Fabry-Perot resonances. (A) A hybrid waveguide consisting of a 0.7 mm of length of 5 µm waveguide coupled to 485 nm waveguide shows the regular fringes of a single-mode waveguide. (B) A single-mode waveguide, 485 nm wide, is shown for comparison. The fringes still contain primarily one period, however there is more noise from increased random reflections.

there is a change in the density of carriers. This effect has been accessed through carrier injection in a p-i-n diode [17], accumulation in a MOS capacitor [18], or carrier depletion in a p-n diode [19].

A cross section of a diode built into a waveguide for optical modulation is shown in Figure 3. This structure is similar to the first high speed p-i-n modulators demonstrated in by Xu in 2005 [17]. The light is confined to the thicker central region of the waveguide, and the thin silicon outside this central region has only a small effect on the optical mode. A diode is formed by doping p-type on the left side of the device, and n-type on the right side of the device. Although similar, this device differs in a few ways from that done by Xu [17]. One difference is that there are a number of doping concentrations in this device. This is done to minimize the electrical resistance near the contacts (far away from the optical mode). Closer to the optical mode, lower doping concentration is necessary to achieve minimal optical loss. Other changes are that the central region of the waveguide is weakly doped n-type, and there is also doping on the sidewalls of the device. These last two changes were made to achieve efficient reverse-bias operation, but have little effect on forward bias operation. Also, compared to Xu [17], all of these results are for Mach-Zehnder interferometer based modulators, (0.5 mm long unless otherwise noted), instead of for a ring resonator structure.

When this device is operated in forward bias, carriers are injected from the p and n regions surrounding the waveguide, increasing the carrier concentration in the weakly doped central region. A detailed analysis of the operation of this device has been provided in reference [20] for devices with no doping in the central region. The performance of this device depends strongly on the carrier lifetime. The carrier lifetime depends on the effective carrier concentration, N, following the formula $\tau=(\tau_0/(1+N/N_0))$, where τ_0 and N_0 are parameters that can determined empirically from the DC characteristics of the device. This device was determined to have τ_0=2.4 ns, and N_0=5×10^{17} cm^{-3}, leading to 3dB bandwidth of 300 MHz
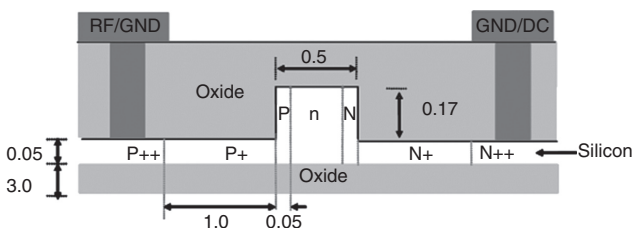
for the device and a switching power of about 3 mW to maintain a π phase shift. A similar device was made with a shorter carrier lifetime by implanting silicon into the central region of the waveguide. The small signal response from this carrier lifetime shortened device (#2) and the original device (#1) are shown in Figure 4, which is reproduced from reference [20]. Shortening the carrier lifetime in the device increases the bandwidth of the device to 2 GHz, but results in lower sensitivity at low frequencies. At frequencies exceeding the 3 dB bandwidth of both devices, there is little difference in their performance. Also shown in Figure 4 are the results of modeling done in reference [20]. There is good agreement between the models and the measurement, except that the analytical model presented in the reference is only valid at lower frequencies. This analytical model fails to capture the complex carrier diffusion and recombination processes that become important at higher frequencies.

The device in Figure 4 can also be operated in reverse bias [21]. When operated in reverse bias, a depletion region forms at the n-type and p-type junction at the edge of the waveguide. Because of the lower carrier concentration in the n-type region, the depletion region is asymmetric, and will extend into the center of the waveguide as the voltage is increased. In comparison to forward bias operation, many fewer carriers are depleted than injected, and, therefore, this device causes a smaller phase shift for a given device length. However, carrier depletion is an intrinsically fast process, and the speed of this device is typically only limited by capacitance. Figure 5 shows the DC operation of devices with lengths of 0.5 and 5 mm. The
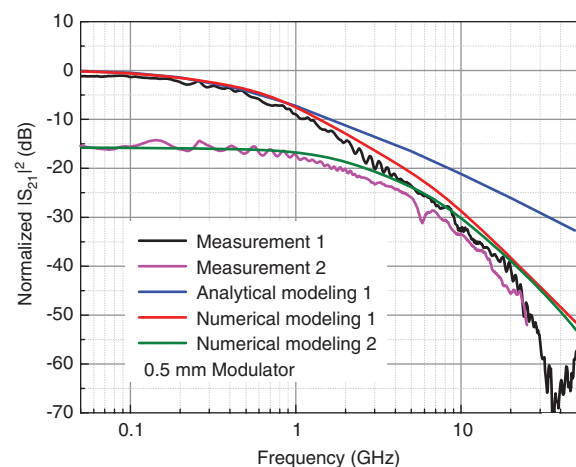

Figure 4 Modeling and measured small signal AC characteristics of the Mach-Zehnder silicon modulator under forward bias with 0.5mm phase shifters. Device #1 is the control device for comparison to device #2 which has its carrier lifetime shortened by implantation with silicon.
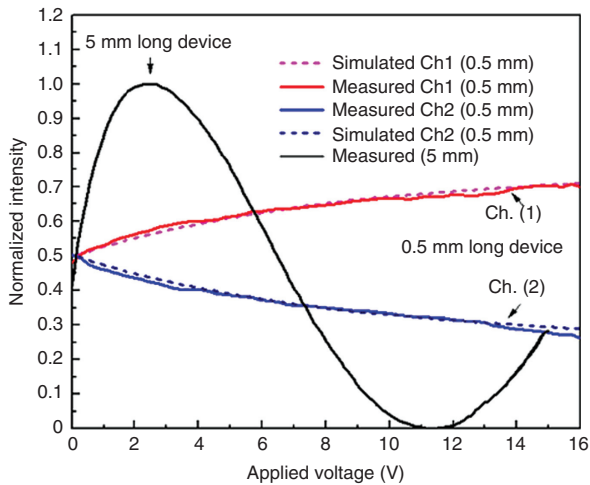

Figure 3 Schematic view of the cross-section of one of a diode based phase shifter. (All dimensions are in μm).

Figure 5 Transmission of light through Mach-Zehnder interferometers with diodes under reverse bias. Shown are devices with active regions 0.5 mm and 5 mm, and only one arm of each interferometer was driven. The 0.5 mm device has two complementary outputs, shown in blue and red.

0.5 mm device is insufficient to cause a π phase shift, but from the 5 mm device a VπL of 4 V·cm can be determined. Figure 6 shows the frequency response of the device, with the performance of the device under forward bias for comparison. Under reverse bias, the bandwidth of the device is 26 GHz. Under forward bias, the device has a much higher response at low frequencies, but the reverse bias device has a greater response at frequencies above 13 GHz.

This device is not optimized for reverse bias operation. In order to optimize the device, a numerical model for performance is developed. The model has three parts: first, the electrical response of the embedded p-n diode is simulated, second this result is used to predict the overall optical response of the phase shifter, and third the
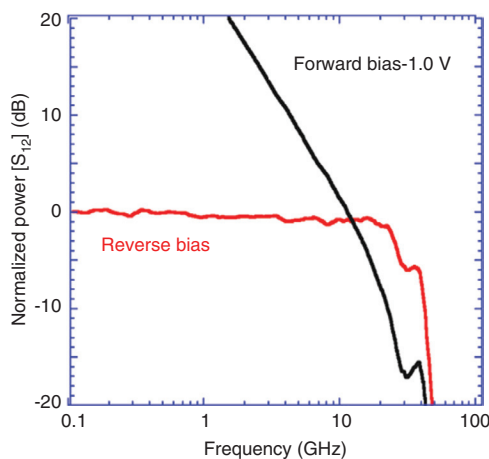

Figure 6 Comparison of the small signal response of a 0.5 mm modulator under reverse and forward bias.

phase sifter response is used to model the complete Mach-Zehnder response. It is worthwhile to note that resonant modulators can be modeled in a similar manner. To model the electrical response of the p-n diode, a commercial program, Synopsis's Sentaurus™ programming suite, is used. Device structures can be created and meshed with either Sentaurus Structure Editor (as a first pass) or Sentaurus Process (to capture the details and nuances of device fabrication). After the device is created, the DC, transient, and AC electrical responses of the device are simulated and cross-sections of the electron and hole distributions are saved. These carrier distributions are then exported to MATLAB where they are converted to index distributions using Soref's equations [15] and input into an optical finite element mode solver. The results of this mode solver give the effective index of the device and the effective loss as a function of voltage (or time or frequency in the case of the transient or AC simulations respectively). The resulting curves are fit to give an analytic equation. The phase change, and loss through a length, L, of the phase shifting device can then be easily calculated, giving an analytic model for the phase-shifting device. This model can be combined with analytic models for the couplers to create a model for the overall Mach-Zehnder structure [22].

Using these simulations one can then optimize the structure described above. The waveguide dimensions, doping concentration and doping location can all be varied. Careful thinking about the problem as well as simulations allow for a few observations. First, the device performance is significantly improved by exchanging the n- and p- type doping locations. Secondly, there is a trade-off between speed and sensitivity with lower speeds yielding higher sensitivities. If the 3dB roll-off point of the reversed-biased diode reduced to ~15 Ghz, sensitivities below 1 V·cm are possible. The speed of the device is set mainly by the doping concentrations and the location of the transition between low and high dopings. For a given doping concentration (and, thus, speed), the sensitivity of the device is maximized when the optical mode is most confined to the area where the depletion width varies with voltage. The location of the junction and the dimensions of the waveguide should be changed to make sure the peak of the mode falls within this region to guarantee maximum shift. From this modeling, we predict that a V_πL of 0.5 Vcm and a speed of 10 Ghz can be achieved in a 700 μm long device [23].

4 All silicon photodiode

The low optical absorption of silicon, at wavelengths near 1.55 μm, makes silicon a useful material for optical

waveguides, but also means that it is a poor material for a photodetector. One method for realizing a photodector on a silicon platform is to introduce another material to provide optical absorption and photocurrent. This is typically epitaxially grown germanium [16, 24], or bonded InGaInAs [25]. Although both materials have been successfully integrated with silicon, both techniques have fabrication challenges. Germanium is easier to integrate, since it is a CMOS compatible material, but the growth of high quality germanium is a non-standard process usually requiring specialized equipment. Another technique that has been used to successfully produce silicon photodectors is the creation of mid-bandgap states directly in the silicon [26]. With the correct implant and anneal, crystal defects can be created to absorb this radiation and generate a photocurrent [27].

Experiments performed by Fan and Ramdas in 1959 using ~1 MeV fast neutrons first demonstrated that defects in damaged silicon can generate photocurrent [28]. Knights in 2003 first demonstrated that the photo response reported by Fan was of practical value [29]. Using Si integrated optics, a pin diode was fabricated in an ion-implanted waveguide that allowed optically generated hole-electron pairs to produce a current. The quantum yield of these devices was fairly low, at only 2%. Reducing the size of the diode increases the efficiency of the photodiode [27], and a quantum efficiency of ~40% of the theoretical maximum at 1.55 μm [30] has been reported by reducing the waveguide structure to submicron geometries.

A photodiode can be made using the same structure as the modulator diode in Figure 3. The only alteration that needs to be made is that the central region will no longer be implanted n-type, and instead will be implanted with Si after the activation anneal. This implant (which is done through 100 nm of oxide) creates crystal defects in the intrinsic region of the pin diode.

A thorough analysis of the character of the crystal defects, based on a review of literature, is provided in [31]. After ion implantation the crystal contains a variety of defects, but even a 15 min anneal a few degrees above room temperature, 50°C, removes many of these defects. Up to anneal temperatures of 300°C, divacancies and vacancy complexes are the dominant type of crystal defect and the largest electrical contributor. Annealing between 300°C and 600°C is believed to repair some vacancies, while some vacancies cluster together. These vacancy clusters are electrically inactive, but the excess silicon forms clusters which are electrically active.

Figure 7 shows the effect of annealing on absorption and photo response of a diode with an ion-implantation
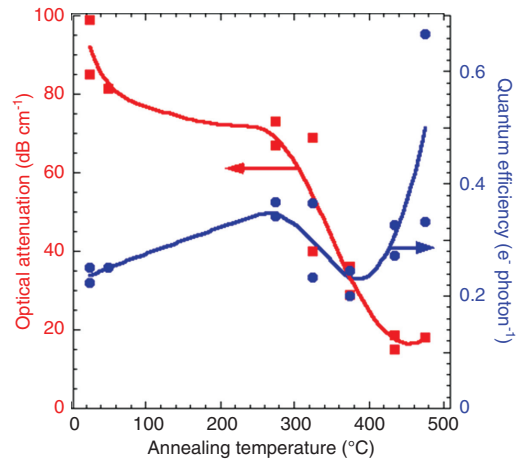

Figure 7 Photodiode quantum efficiencies of 1550 nm light at 5 V bias as a function of annealing temperature after defect formation by 1013-cm^{-2} 190-keV Si+ implantation. For temperatures 25–435°C annealing was in vacuum, <5×10-4 Pa, for ~15 min. The 475°C anneal was in flowing nitrogen for 2 min. The curves are drawn to follow the data points.

dose of 10^{13} Si$^+$ cm^{-2}. Note that the quantum efficiency is defined as electrons per absorbed photon, and is independent of the length of the device that may be required to absorb the photons. At lower temperatures, where the divacancies are a dominant type of defect, the optical absorption is relatively large. As the annealing temperature is increased past 300°C, the number of vacancies decreases, and the absorption goes down, leveling off at temperature near 450°C. With one notable exception, the quantum efficiency is relatively constant in this anneal temperature range. The efficiency increases slightly as the anneal temperature is increased to 300°C, perhaps due to the removal of electrically inactive, but optically absorbing defects. One sample, annealed at 475°C, demonstrated significantly higher quantum efficiency than all other samples. Unlike the other samples represented on this graph, this sample was annealed in nitrogen for 2 min instead of a vacuum for about 15 min. It is possible that the difference in annealing is responsible for the difference in quantum efficiency; however the higher quantum efficiency has proven difficult to reproduce.

Table 1 summarizes a number of measured parameters, from photodiodes fabricated under different conditions. The photodiodes implanted to 10^{13} cm^{-2} and annealed to 475°C have been discussed in [27], and exhibit two stable states, L_1 and L_2. After fabrication the diode is in the L_1 state. If the diode is forward biased for a few minutes with a current per diode length >100 mA cm^{-1}, then the diode is transformed to the L_2 state. The process is reversed by heating the diode to 250°C in air for a few

Table 1 Summary of the performance of all-silicon photodiodes with different implant and anneal conditions.

Dose	L State	Anneal Temp	Optical absorption	QE at 2V	QE at 5V	QE high V (V)	Dark current (5 V)
10^{13} Si$^+$ cm^{-2}		<300°C	70 dB/cm	0.15	0.2	3 (20 V)	28 nA
10^{13} Si$^+$ cm^{-2}	L$_1$	475°C	8 dB/cm	0.5	0.6	1 (20V)	0.12 nA
10^{13} Si$^+$ cm^{-2}	L$_2$	475°C	18 dB/cm	0.6	0.6	5 (20V)	2.6 nA
10^{14} Si$^+$ cm^{-2}		475°C	90 dB/cm	0.01	0.03	0.3 (12V)	
10^{14} Si$^+$ cm^{-2}		600°C	70 dB/cm	0.1	0.15	1 (12V)	25 nA (6V)

seconds. At low bias voltages, the quantum efficiencies for both states are similar, however, the L$_2$ state has significantly higher optical absorption.

Also shown in Table 1 is the performance of the photodiodes under different reverse bias voltages. At lower voltages (up to 5 V), diodes implanted with minimal annealing, <300°C, exhibit a significant increase in quantum efficiency with bias voltage. The increase in quantum efficiency with bias voltage may be the result of field-enhanced ionization [32]. At higher voltages, many of the devices begin to avalanche, and can exhibit quantum efficiencies >1.

Table 1 also includes data from photodiodes that had a higher implant dose of 10^{14} Si$^+$ cm^{-2}. With an anneal temperature of 475°C, these devices exhibit photocurrent that is extremely dependent on bias voltage, and such devices are of limited practical value. When a higher anneal temperature of 600°C is used, this device performs very similarly to the lower dose, lower temperature anneal case. The dark currents (given for 1 mm lengths) for all devices are fairly small, although the dark current was best for the 10^{13} Si$^+$ cm^{-2} dose and 475°C implant.

Photodiodes implanted to 10^{13} cm^{-2} and annealed to 475°C exhibit a frequency response >35 GHz and a transient response <13 ps. However, these high frequency measurements were made on a 0.25-mm-long photodiode, which only absorbs ~10% of the incoming light even in the L$_2$ state. If it is required to absorb 90% of the incoming light then the diode must be 6 mm long and the transit time of light through the diode is ~90 ps. However, since the light exponentially decreases in intensity as it moves through the diodes the effective pulse width is ~30 ps resulting in a frequency response ~5 GHz.

5 Ring resonator based filters

Another important component in many optical systems is a wavelength selective filter. There are a number of ways to realize wavelength filters in an integrated silicon photonics platform, such as arrayed waveguide gratings (AWG) [33], echelle gratings [34], Mach-Zehnder interferometer chains [35], and ring resonators. We have focused on ring resonator filters because of their compactness, low insertion loss, adaptability to many different bandwidth requirements, and ease of implementation. One characteristic of ring resonator filters is that they concentrate the light and are, therefore, sensitive to nonlinearities. This has made ring resonators a method to use when non-linearities are desired, such as in a parametric oscillator [36]. As will be discussed, however, this can limit the power handling capabilities of ring resonator filters for some applications.

A ring filter is somewhat analogous to a Fabry-Perot resonator, and the equations that determine transmission, free-spectral range, and finesse, for a Fabry-Perot resonator [37] can also be used to determine the performance of a ring resonator containing a single ring. To improve the performance of a filter it is possible to use multiple coupled rings inside of the filter as described by Little [38]. The use of multiple coupled rings can created filters with steeper frequency roll-off, and flatter filter shapes.

The design and fabrication of a ring resonator requires precise control of the path length of the ring and the optical couplings while, minimizing optical loss. Typically, it is very difficult, if not impossible, to achieve the desired control of the resonant wavelength of a ring filter by accurate fabrication of the waveguide, alone. A filter design may call for control of the wavelength by 1 pm to 100 pm, and the fabrication tolerance required to achieve this is of similar scale. It should be noted that there has been some efforts and success in achieving such dimensional control [39].

A perhaps better method for accurately controlling the wavelength of the filter is to alter the optical path length after the fabrication of the ring. Post fabrication trimming has been demonstrated by altering the dimensions of a silicon nitride cladding [40] or by lithographic exposure of a waveguide cladding [41]. Even with post-fabrication trimming, thermal control of a filter is necessary. Silicon has a thermal coefficient of refractive index of

dn/dt=1.8×10⁻⁴ K⁻¹. For a typical device, the resonant wavelength changes by about 0.1 nm for every degree change in temperature.

The sensitivity of silicon to temperature means that temperature can also be used as an efficient means of changing the wavelength of a filter after fabrication. Thermal tuning is done by adding electrically resistive heaters, typically either above the ring filter [42] or in silicon adjacent to the ring filter [43]. In most cases, every ring requires its own heater, to allow independent tuning.

Figure 8 shows the silicon waveguide layer for a ring resonator with two coupled rings. The size of the waveguide in the ring is 450 nm×210 nm and the ring diameter is close to 4.6 μm. This ring resonator was designed for a filter bank with a channel spacing of 150 GHz and 30 dB of extinction. The filter used polysilcon heaters above the rings, for tuning. The performance of this filter bank was unsatisfactory. Many of the channels have high insertion loss, and some of the channels have irregularly shaped pass-bands. Both of these problems are due to excess scattered light from sidewall roughness. The scattered light creates both loss (due to light scattered out of the waveguide) and irregular pass-bands (due to light backscattered in the waveguide) [8].

To improve the filter performance, the amount of sidewall scattered light needs to be lowered. This can be done by creating smoother sidewalls by reflowing the photoresist using a post-development bake before pattern transfer into the silicon layer. Reflowing the photoresist enough to increase the waveguide dimensions by 50 nm was shown to reduce the sidewall roughness from about 2 nm rms to 1 nm rms. This method was used to produce a 3 channel filter with 3 dB insertion loss and regular pass-bands [4]. The reflowing technique, however, is not ideal because it can increase the dimensional variation of the fabricating
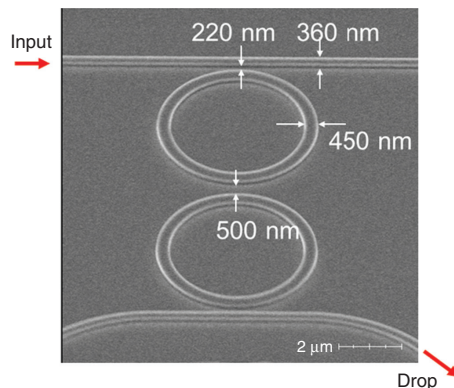
filter, which increases the power necessary to tune a filter bank.

Another method for lowering the unwanted scattering of light is to use a thinner waveguide. A thinner waveguide has smaller effective index contrast, which allows a wider single-mode waveguides to be used. By lowering the index contrast and widening the waveguide, the amount of light that is scattered is greatly reduced. Figure 9 shows the optical image of part of a completed pair of filter banks fabricated using 600 nm×115 nm silicon waveguides, and the ring size in these filters is ~13 μm in diameter. Figure 10 shows the performance of this pair of filter banks, each with 20 channels, after tuning. The two filter banks achieve nearly identical performance, and all channels achieve the desired extinction of 30 dB with a spacing of 80 GHz. Most channels have insertion loss <2 dB, and the worst channel has a loss of 3 dB. Figure 11 shows the location of the resonant frequencies before and after tuning. Most channels need 1–2 nm of tuning.

Although effective, thinning the silicon waveguide layer does have some drawbacks. Lowering the lower effective index contrast for a waveguide will increase the minimum possible bending radius. Thinner waveguides require larger rings, and this limits how large of a FSR is possible. In the two cases above, the thick rings had a FSR of 5.0 THz and the thin rings had a FSR of 2 THz. Thinner silicon also puts more of the mode outside of the silicon, lowering the temperature sensitivity of the resonant frequency of the waveguide. Together with the larger size of the ring, this means significantly more power is needed to tune the ring. The thick rings described above required 1.0 mW/nm for tuning, while the thin rings required 2.6 mW/nm. The thinner geometry is also very sensitive to the exact thickness of the silicon. The thinner silicon geometry, however, is a little less sensitive to lateral dimensional changes.
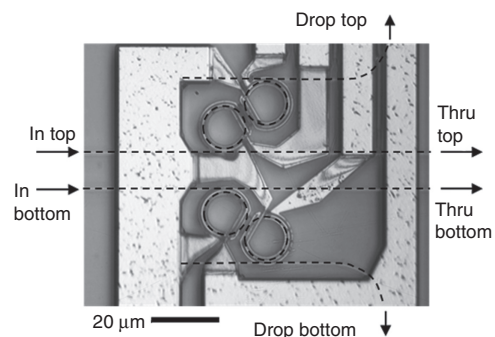

Figure 8 The waveguide layer from a filter with two coupled rings. Dimensions are labeled, and the input and drop ports are also shown.

Figure 9 An optical image of one channel in a pair of nominally identical filter banks. The waveguides are hidden by the wiring for the heaters, and are drawn in with dashed lines.
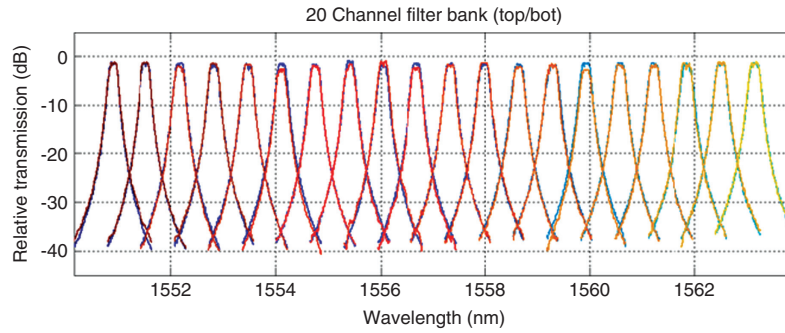
Figure 10 Drop-port transmission characteristics of the filter banks after tuning. The blue-green colors are the top bank, and the red-orange yellow colors are the bottom bank. Because the data from the two filter banks match well, the data from the top bank is largely hidden behind the data from the bottom bank.

6 Linear performance

For an optical system, particularly one that deals with analog signals, linear performance is often important. In a simple optical link, three sources of non-linearity should be considered: signal encoding, signal transmission (including filtering or any optical signal processing), signal detection. Linearity in detectors is not unique to silicon, and will not be discussed here.

The transmission of light through silicon waveguides can produce significant non-linearity. The tight confinement of a silicon waveguide means that light is highly concentrated in the waveguide, and large intensities of light are reached even with modest optical powers. In a resonate filter, light is further concentrated. The filter in the previous section, with a 4.6 μm diameter, has an intensity of light 170 times greater in the filter than at the input waveguide. For a 1 mW input into the filter, the flux density in the filter is approximately 3×10^8 W/cm^2.

Two-photon absorption (TPA) is one of the mechanisms for the non-linear response of silicon, with a non-linear β value of 1 cm/GW near 1550 nm [44]. TPA directly causes non-linear absorption, however, the free carriers

generated by TPA are often of greater concern. The carriers generated by TPA absorb light, and will also change the index of the silicon, shifting the resonance of a filter. These processes also generate heat, which along with heat generated through linear material absorption, can further shift the resonance of a filter. These three effects (TPA, free-carriers, thermal) all occur with different time-scales. TPA is nearly instantaneous, free-carriers typically have lifetimes on the order of ns in silicon waveguides, and thermal effects have time constants of a few μs.

To measure the non-linearity of a signal propagating through a silicon filter, two-tone measurements have been used [45]. The measurements were made on the drop signal using a single ring filter that was similar to the 4.2 μm diameter double ring filter measured in the previous section. This filter was fabricated using the resist reflow process and had a Q of 20,000. Figure 12 shows the non-linear performance of the ring when measured at different frequencies and with different optical powers. At lower frequencies, near 10 MHz, the non-linearity is quite severe. At these frequencies, the absorption and phase shifting from the TPA generated carriers causes a non-linear response of the ring filter. At higher frequencies, such as 1 GHz, the
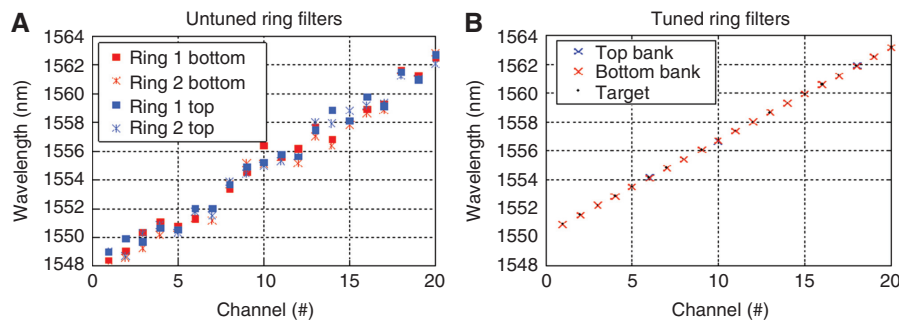

Figure 11 (A) Resonant wavelengths for the rings as-fabricated with no power in heaters. There are two filter banks (top and bottom), with two coupled rings each, for a total of four rings at each channel. (B) Center wavelengths for the filters after tuning.
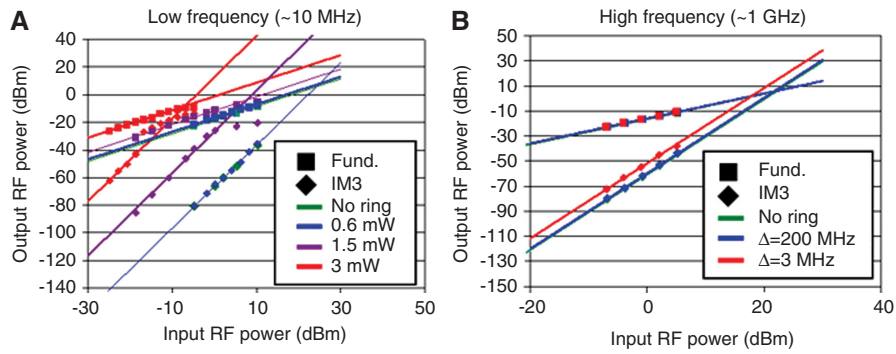
Figure 12 Measurements of a two-tone signal through a ring resonator. (A) Data was taken at frequencies of f1=10 MHz, and f2= 13 MHz. The points are the data, and the straight lines are fits that assume a slope of 1 for the fundamental and a slope of 3 for IM3. At higher optical and RF powers, the behavior of the ring becomes more complicated, and the measurements no longer follow the usual slopes. The data that diverges is not used in calculating the fit. (B) Data was taken at a fixed optical power of 13 mW and at frequencies of 1000 and 1200 MHz for the Δ=200 MHz case, and 1000 and 1003 MHz for the Δ=3 MHz case.

period of the signal is far shorter than the carrier lifetime, and the carriers cannot respond. The response of the ring is therefore much more linear. There is still a small non-linear degradation of the signal if the difference between the frequencies of the two tones is small. This is due to the fact that the two-photon generation of carriers is a non-linear process, and therefore carriers are generated at the intermodulation or beat frequencies.

There are also other important non-linear effects. Thermal heating of the ring, primarily due to linear material absorption, can start to shift the resonance of the ring at constant wave (CW) optical powers as low as 100 μW. At higher powers, the two photon generated carriers create enough loss that the transmission and Q of the ring become limited. In the above ring, as the CW optical power is increased above 1 mW, carrier absorption increases the loss such that the optical power at the output increases very little, and is effectively clamped at an output near 1 mW.

In an optical system, non-linearity can also occur at the encoding stage. An ideal Mach-Zehnder interferometer with perfectly linear, loss-less phase shifters, for example, has a sinusoidal response to a phase change, not a linear one. Reversed-biased silicon phase shifters are neither linear nor loss-less. Because of this, one must carefully choose the modulator design and operation point to ensure operation is linear enough for the desired application. In particular, for analog applications, a high degree of linearity is often important, and linearity is often limited by the optical modulator [46]. Many schemes have been proposed to create more linear modulators (see for example [46, 47] and [48]). These schemes can generally be split into two different categories: electrical schemes (such as pre-emphasis, feedback schemes, and post-processing fixes) and optical schemes (cascaded MZ modulators, splitting and recombining signals, adding

other optical elements). However, these techniques lead to extra complexity in the system as well as other, scheme specific, drawbacks. We have proposed in [49] a simple linearization scheme that uses the non-linearity of the silicon phase-shifter to cancel the nonlinearity of the Mach-Zehnder modulator.

To understand how this works we write out the Mach-Zehnder transfer-function and Taylor expand around a given voltage point to get:

$$P_{top} \approx P_0 e^{-\alpha_{DC}L}\left[\frac{1}{2}+(aL)v+\frac{1}{4}(x^2L^2\text{-}yL)v^2+\left(-\frac{2}{3}a^3L^3+\frac{c}{6}L\text{-}\frac{1}{2}ayL^2\right)v^3\right]$$

where P_{top} is the output power, P_0 is the input power, v is the voltage applied to the phase shifter, L is the length of the phase-shifter, a, b, and c are the coefficients of the expansion of the index change such that the phase-shift, φ, is given by: $\varphi(v) \approx \left(\varphi_{DC}+av+\frac{bv^2}{2}+\frac{cv^3}{6}\right)L$, and x,y, and z are the equivalent for the loss such that: $\alpha(v) \approx \left(\alpha_{DC}+xv+\frac{yv^2}{2}+\frac{zv^3}{6}\right)L$ [49]. In this calculation, we have assumed that the modulator is biased in quadrature and the arms are exactly balanced. The first two terms in this equation are a DC offset and the desired linear response. The second two terms are the second and third-order nonlinearity. The second order nonlinearity (and, indeed, all even order non-linearities) can be canceled out by using differential detection. Tuning the heater bias of the modulator can also cancel the second harmonic alone. The third order non-linearity can be canceled by choosing the length and DC bias voltage such that $L=\frac{1}{4a^2}\left(\frac{\text{-}3y}{2}\pm\sqrt{\frac{9y^2}{4}+4ca}\right)$ and the coefficient in front of the v^3 term is zero. In practice, the bias voltage
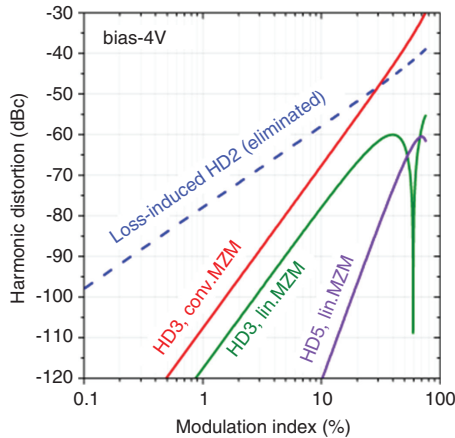
Figure 13 Harmonic distortion in linearized modulator.

can be tuned to correct for fabrication variations and for the extra terms in the third harmonic from higher order nonlinearities. Canceling the second and third order harmonics of the device is usually sufficient to ensure nicely linear operation as higher harmonics are generally below the noise floor. Figure 13 shows numerically predicted linearity results for a 312 μm long device operated at 4V DC bias. The next highest harmonic (the fifth harmonic) and the third harmonic for the case of a Mach-Zehnder with perfectly linear loss-less phase-shifters are included for reference. As can be seen, a predicted linearity of better than 60 dBc is obtained, more than 20 dBc better than the "ideal" case at high modulation depths.

7 Hybrid (photonic and electronic) analog-to-digital converter

The components described above have been integrated together for the photonic front end of an analog-to-digital converter (ADC) [4]. The accuracy and speed of an ADC are fundamentally limited by the aperture jitter that can be achieved. To avoid this limitation, a mode locked-laser is used to sample a signal with much lower jitter than most electronic timing sources. In addition, a wavelength division multiplexing method, as done by Yariv [50] and Kang [51], is used to divide the sampled signals among multiple electronic ADCs to sample the signal at a slower rate.

Figure 14 schematically shows the method used for the optical sampling. The precisely timed pulses created by a mode-locked laser are narrow, and therefore have a broad spectrum. The pulses are spectrally separated and each color has a different time delay. The colors are then recombined and the light is put through a single modulator which encodes the signal to be sampled. Each color arrives at the modulator at a different, but precisely known time. After the modulator the colors are separated again, and the light reaches an array of photodetectors connected to an array of electronic ADCs. The signal can then be reconstructed digitally by interweaving the data from the separate ADCs. It is possible to use the two complementary outputs of the modulator (doubling the number of filter channels and electronic ADCs) to increase the accuracy of the sampling and reject variations in the data due to laser amplitude changes [52]. Although the chip was fabricated with this capability, the capability was not used because other sources of noise were greater.

For this demonstration, only the modulator and the photonic components after the modulator (the filter bank and detectors) were integrated using silicon photonics. The components before the modulator were discrete components in this demonstration. It should be noted that all of these components are straight-forward to integrate using silicon photonics, except for the mode-locked laser. The modulator used was of the type shown in Figure 3 with diodes 0.5 mm long. This device has a somewhat
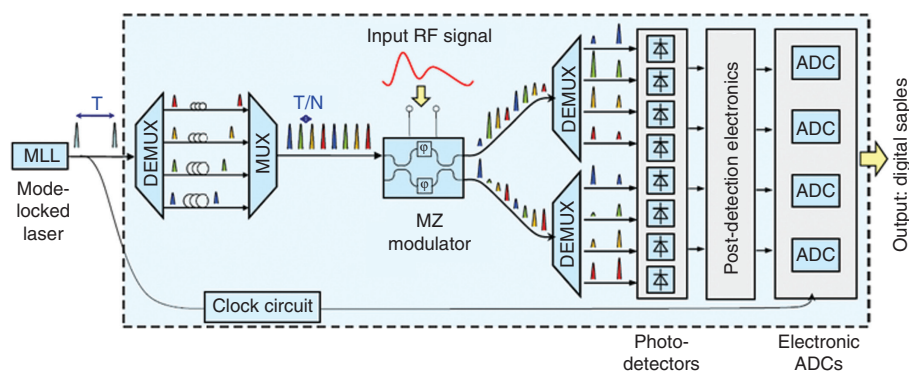

Figure 14 Layout of the photonic ADC. In the referenced work, the silicon chip comprised the modulator, demultiplexers, and photodetectors, while all other components were implemented off-chip.
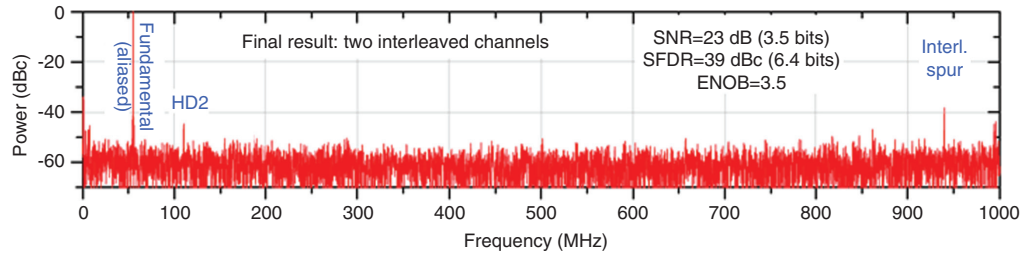
Figure 15 Data measured with two 1.05 GSa/s channels of the photonic ADC based on an integrated silicon photonic chip. This ADC was used to digitize a 10 GHz RF signal and the Fourier transform of the interleaved data is shown.

poor $V\pi$ of 40 V when driven in a push-pull configuration. The filters were described earlier and use a 210 nm thick layer of silicon patterned using the reflowed resist process. The photodiodes were implanted with silicon with an area dose of 10^{14} cm^{-2} and annealed at $600°C$. These diodes were 0.5 mm long, and had an efficiency of 0.1 A/W.

The photonic ADC was used to sample a signal with a single tone near 10 GHz. This demonstration only sampled with two channels, and each electronic ADC sampled at 1.05 Gs/s. This therefore limits the sampling rate to 2.1 Gs/s and the 10 GHz signal is aliased down to 1 GHz band. (20 Channels would be necessary to sample a full 10 GHz of bandwidth). This method still measures the ability of the photonic ADC to accurately sample a 10 GHz signal, even if it does not capture the full 10 GHz of bandwidth.

Figure 15 shows the spectrum from the sampling of this single tone. Visible are the fundamental frequency near 50 MHz, the second harmonic near 100 MHz, and an interleaving spur near 950 MHz. In the absence of noise, the spur-free dynamic range is 39 dBc (or 6.4 bits, equivalent). The noise floor, however, gives a signal-to-noise ratio (SNR) of 23 dB (or 3.5 bits equivalent). This poor SNR is due to the losses in the optical system and the poor sensitivity of the photodiodes. If the sampling is done using no filters, and the output of the mode-locked laser is left as a single pulse, the increase in signal improves the SNR to 38 dB.

8 Conclusion

Silicon photonics have been successfully demonstrated by many groups, and it is no longer in doubt that the devices can perform as necessary for many applications. The next step is getting silicon photonics to be the technological choice for applications. It is natural to ask what is preventing the widespread use of silicon photonics. Cost and availability has been a factor, but that is likely to change due to the availability of silicon photonics fabrication through

services such as OPSIS and ePIX. These services, which also provide design kits, could be expected to increase the accessibility of silicon photonics to more research groups and perhaps lower the cost of fabrication.

Perhaps the most important limitation to silicon photonics technology is the lack of an inherent optical source. Optical gain has been achieved in a silicon system by the incorporation of other materials. For electrically pumped sources, methods include hybrid integration of III-V [53] and germanium lasers [54]. III-V integration requires non-standard and challenging fabrication steps, negating many of the benefits of silicon photonics technology over an all III-V photonics technology. Germanium lasers, while an important advancement, still need a fair amount of further development before they are likely to be widely incorporated. Over time, these technologies can be expected to improve, but in the near term, silicon photonics will likely be used primarily for systems where off-chip optical gain is sufficient.

The power handling capability of silicon photonics can also be an important limitation. For some applications, particularly analog signal applications, high optical powers can be necessary [55]. For example, the accuracy of a photonic ADC is limited both by the power that reaches the photodiode and the uncorrectable non-linearity of the modulator. As discussed, the non-linearity of the modulator can be improved by carefully design of the doping of the modulator. It is possible for a silicon modulator to give better linearity than a Mach-Zender modulator with a perfect phase shifter. As also discussed, the ring resonator design currently being used in the ADC has a practical maximum CW power of 1 mW. In the photonic ADC the power is spread among 20 channels, and an average power of 10 mW should be possible. This limits the best theoretical SNR that can be achieved to an equivalent of nearly 10 bits at 10 GHz if we consider only the noise from photon statistics.

The choice of filter for the above measurements was a particularly sensitive case. Because of the compactness and the high Q of the filter, the light in the ring is 170 times

more intense in the ring than in the input waveguide. Larger rings and thinner silicon would cause the non-linearity effects to occur at higher powers, without having to sacrifice the Q of the resonator. Replacing the ring filter with a different design, or substituting an arrayed-wave-grating design should allow power levels up to 100 mW, increasing the possible resolution slightly to 10.5 bits at 20 GHz in a perfect system. This power level is optimistic, because in a fully integrated photonic chip, a similar filter bank will also be needed to separate the light directly from the mode locked laser. The power handling capability of this first filter, and the losses after this filter will likely limit the power that can reach the photodiodes.

An important remaining challenge for silicon photonics is the challenge in controlling the resonant frequencies in a filter bank. As a platform, silicon photonics is likely to be most useful for the integration of a large number of devices, and none of the current methods for tuning the resonant frequencies of a filter have been scaled to a large number of devices. Post-fabrication trimming methods require cycles of measurement and physical alteration, and likely cannot be done quickly enough for high volume manufacturing. Thermally tuning will require electronic control of the temperature of every ring. Feedback (either optically or temperature based) will likely be necessary, and the required electronics could be extensive. Although there are demonstrations of automated thermal control of single rings [56], a demonstration of the simultaneous thermal control of a large number of filters, has not yet occurred. Because of the miniaturization of electronics, the need for extensive electronics is not necessarily an insurmountable problem. Besides the engineering challenges, however, a fundamental problem with thermal tuning is the relatively large amount of power it can require. Designs have been demonstrated that reduce the tuning power by a factor of 2 compared to the best filters in the above section [43].

Even with these challenges, there are still many problems that can be solved by silicon photonics, as the technology stands today. One example, the front end of an A/D converter was described here in detail. This is just one example, and there are a number of possible applications [1, 6, 57], which are suitable for silicon photonic solutions in the very near future.

References

[1] Koch B, Alduino A, Liao L, Jones R, Morse M, Kim B, Lo W-Z, Basak J, Liu H-F, Rong H, Sysak M, Krause C, Saba R, Lazar D, Horwitz L, Bar R, Litski S, Liu A, Sullivan K, Dosunmu O, Na N, Yin T, Haubensack F, Hsieh I-w, Heck J, Beatty R, Bovington J, Paniccia MJ. A 4×12.5 Gb/s CWDM Si photonics link using integrated hybrid siicon lasers. Paper presented at: CLEO: 2011 - Laser Science to Photonic Applications, 2011; Baltimore.

[2] OpSIS. 2013 (Accessed on June 1, 2013 Available at: http://opsisfoundry.org/.)

[3] Pozo J, Kumar P, Cascio D, Khanna A, Dumon P, Delbeke D, Baets R, Fournier M, Fedeli J, Fulbert L, Zimmermann L, Tillack B, Tian H, Aalto T, O'Brien P, Deptuck D, Xu J, Zhang X, Gale D. Essential: EPIXfab services specifically targeting (SME) industrial takeup of advanced silicon photonics. Paper presented at: 14th International Conference on Transparent Optical Networks (ICTON), 2012; Coventry.

[4] Khilo A, Spector SJ, Grein ME, Nejadmalayeri AH, Holzwarth CW, Sander MY, Dahlem MS, Peng MY, Geis MW, DiLello NA, Yoon JU, Motamedi A, Orcutt JS, Wang JP, Sorace-Agaskar CM, Popovic MA, Sun J, Zhou G-R, Byun H, Chen J, Hoyt JL, Smith HL,

Ram RJ, Perrott M, Lyszczarz TM, Ippen EP, Kärtner FX. Photonic ADC: overcoming the bottleneck of electronic jitter. Opt Express 2012;20:4454–69.

[5] Xia B, Chen LR. Arbitrary optical waveform generation using 2D ring resonator arrays. Opt Express 2006;14:6619–27.

[6] Tu K-Y, Rasras MS, Gill DM, Patel SS, Chen Y-K, White AE, Pomerene A, Carothers D, Beattie J, Beals M, Michel J, Kimerling LC. Silicon RF-photonic filter and down-converter. J Lightwave Technol 2010;28:3019–28.

[7] Povinelli ML, Johnson SG, Lidorikis E, Joannopoulos JD, Soljacic M. Effect of a photonic band gap on scattering from waveguide disorder. Appl Phys Lett 2004;84:3639–41.

[8] Borselli M, Johnson TJ, Painter O. Beyond the Rayleigh scattering limit in high-Q silicon microdisks: theory and experiment. Opt Express 2005;13:1515–30.

[9] Lee KK, Lim DR, Kimerling LC, Shin J, Cerrina F. Fabrication of ultralow-loss Si/SiO2 waveguides by roughness reduction. Opt Lett 2001;26:1888–90.

[10] Biberman A, Shaw MJ, Timurdogan E, Wright JB, Watts MR. Ultralow-loss silicon ring resonators. Opt Lett 2012;37:4236–8.

[11] Cardenas J, Poitras CB, Robinson JT, Preston K, Chen L, Lipson M. Low loss etchless silicon photonic waveguides. Opt Exp 2009;17:4752–7.

[12] Bauters JF, Heck MJR, John DD, Barton JS, Bruinink CM, Leinse A, Heideman RG, Blumenthal DJ, Bowers JE. Planar waveguides with less than 0.1 dB/m propagation loss fabricated with wafer bonding. Opt Exp 2011;19:24090–101.

[13] Lee KK, Lim DR, Luan HC, Agarwal A, Foresi J, Kimerling LC. Effect of size and roughness on light transmission in a Si/SiO2 waveguide: Experiments and model. Appl Phys Lett 2000;77:1617–9.

[14] Spector SJ, Geis MW, Lennon DM, Williamson RC, Lyszczarz TM. Hybrid multi-mode/single-mode waveguides for low loss. Paper presented at: Integrated Photonics Research Topical Meetings, 2004, Washington, DC.

[15] Soref RA, Bennett BR. Electrooptical Effects in Silicon. IEEE J Quant Electron 1987;23:123–9.

[16] Liu J, Camacho-Aguilera R, Bessette JT, Sun X, Wang X, Cai Y, Kimerling LC, Michel J. Ge-on-Si optoelectronics. Thin Solid Films 2012;520:3354–60.

[17] Xu Q, Schmidt B, Pradhan S, Lipson M. Micrometre-scale silicon electro-optic modulator. Nature 2005;435:325–7.

[18] Liu A, Jones R, Liao L, Samara-Rubio D, Rubin D, Cohen O, Nicolaescu R, Paniccia M. A high-speed silicon optical modulator based on a metal-oxide-semiconductor capacitor. Nature 2004;427:615–8.

[19] Liao L, Liu A, Rubin D, Basak J, Chetrit Y, Nguyen H, Cohen R, Izhaky N, Paniccia M. 40 Gbit/s silicon optical modulator for high speed applications. Electron Lett 2007;43:1196–7.

[20] Zhou GR, Geis MW, Spector SJ, Gan F, Grein ME, Schulein RT, Orcutt JS, Yoon JU, Lennon DM, Lyszczarz TM, Ippen EP, Kärtner FX. Effect of carrier lifetime on forward-biased silicon Mach-Zehnder modulators. Opt Exp 2008;16:5218–26.

[21] Spector SJ, Geis M, Zhou GR, Grein ME, Gan F, Popovic MA, Yoon JU, Lennon DM, Ippen EP, Kärtner FX, Lyszczarz TM. CMOS-compatible dual-output silicon modulator for analog signal processing. Opt Exp 2008;16:11027–31.

[22] Sorace-Agaskar C. Advanced Silicon Photonic Modulators, S. M. Thesis. Cambridge: Massachusetts Institute of Technology, 2010.

[23] Spector SJ, Sorace CM, Geis MW, Grein ME, Yoon JU, Lyszczarz TM, Ippen EP, Kartner FX. Optimization of silicon-diode-based optical modulators. Selected Topics in Quant Electron 2010;16:165–72.

[24] DeRose CT, Trotter DC, Zortman WA, Starbuck AL, Fisher M, Watts MR, Davids PS. Ultra compact 45 GHz CMOS compatible Germanium waveguide photodiode with low dark current. Opt Exp 2011;19:24897–904.

[25] Fang AW, Jones R, Park H, Cohen O, Raday O, Paniccia MJ, Bowers JE. Integrated AlGaInAs-silicon evanescent racetrack laser and photodetector. Opt Exp 2007;15:2315–22.

[26] Geis MW, Spector SJ, Grein ME, Schulein RT, Yoon JU, Lennon DM, Deneault S, Gan F, Kaertner FX, Lyszczarz TM. CMOS-compatible all-Si high-speed waveguide photodiodes with high responsivity in near-infrared communication band. IEEE Photon Technol Lett 2007;19:152–4.

[27] Geis MW, Spector SJ, Grein ME, Schulein RT, Yoon JU, Lennon DM, Wynn CM, Palmacci ST, Gan F, Kärtner FX, Lyszczarz TM. All silicon infrared photodiodes: photo response and effects of processing temperature. Opt Exp 2007;15:16886–95.

[28] Fan HY, Ramdas AK. Infrared absorption and photoconductivity in irradiated silicon. J Appl Phys 1959;30:1127–34.

[29] Knights A, House A, MacNaughton R, Hopper F. Optical power monitoring function compatible with single chip integration on silicon-on-insulator. Conference on Optical Fiber Communication, Technical Digest Series 2003;86:705–6.

[30] Logan DF. Defect-enhanced silicon photodiodes for photonic circuits. Doctor of Philosophy Thesis: McMaster University, 2011.

[31] Geis MW, Spector SJ, Grein ME, Yoon JU, Lyszczarz TM. Near-infrared silicon photodetectors. In: Handbook of silicon photonics. Abington: Taylor and Frances Inc, 2013, pp. 512–29.

[32] Yong Z, Chao X, Wan-Jun W, Qiang Z, Yin-Lei H, Jian-Yi Y, Ming-Hua W, Xiao-Qing J. Photocurrent effect in reverse-biased p-n Silicon waveguides in communication bands. Chinese Phys Lett 2011;28:74216–9.

[33] Fang Q, Li F, Liu Y. Compact SOI arrayed waveguide grating demultiplexer with broad spectral response. Opt Commun 2006;258:155–8.

[34] Horst F, Green WMJ, Offrein BJ, Vlasov YA. Silicon-on-insulator echelle grating WDM demultiplexers with two stigmatic points. IEEE Photon Technol Lett 2009;21:1743–5.

[35] Yu H, Chen M, Li P, Yang S, Chen H, Xie S. Silicon-on-insulator narrow-passband filter based on cascaded MZIs incorporating enhanced FSR for downconverting analog photonic links. Opt Exp 2013;21:6749–55.

[36] Saha K, Okawachi Y, Levy JS, Lau RK, Luke K, Foster MA, Lipson M, Gaeta AL. Broadband parametric frequency comb generation with a 1-μm pump source. Opt Exp 2012;20:26935–41.

[37] Born M, Wolf E. Principles of optics, sixth edition. Elmsford: Pergamon Press Inc., 1980.

[38] Little BE, Chu ST, Haus HA, Foresi J, Laine JP. Microring resonator channel dropping filters. J Lightwave Technol 1997;15:998–1005.

[39] Holzwarth C, Barwicz T, Popovic M, Rakich P, Ippen E, Kärtner F, Smith HI. Accurate resonant frequency spacing of microring filters without postfabrication trimming. J Vacuum Sci Technol B: Microelectron Nanometer Struct 2006;24:3244–7.

[40] Atabaki AH, Askari M, Eftekhar AA, Adibi A. Accurate post-fabrication trimming of silicon resonators. Paper presented at: IEEE International Conference on Group IV Photonics GFP, 2012, San Diego.

[41] Canciamilla A, Grillanda S, Morichetti F, Ferrari C, Hu J, Musgraves JD, Richardson K, Agarwal A, Kimerling LC. Photo-induced trimming of coupled ring-resonator filters and delay lines in As2S3 chalcogenide glass. Opt Lett 2011;36:4002–4.

[42] Spector SJ, Khilo A, Peng M, Kartner FX, Lyszczarz TM. Thermally tuned dual 20-channel ring resonator filter bank in SOI (silicon-on-insulator). Paper presented at: 2011 Conference on Lasers and Electro-Optics: Laser Science to Photonic Applications, CLEO 2011, 2011, Baltimore.

[43] Watts MR, Zortman WA, Trotter DC, Nielson GN, Luck DL, Young RW. Adiabatic resonant microrings (ARMs) with directly integrated thermal microphotonic. Paper presented at: 2009 Conference on Lasers and Electro-Optics and 2009 Conference on Quantum Electronics and Laser Science Conference, CLEO/QELS 2009, 2009, Baltimore.

[44] Bristow AD, Rotenberg N, Driel HMv. Two-photon absorption and Kerr coefficients of silicon for 850–2200 nm. Appl Phys Lett 2007;90:191104–3.

[45] Spector SJ, Yegnanarayanan S, Swint RB, Lyszczarz TM, Juodawlkis PW. Two-tone measurement of the nonlinear behavior of a silicon-on-insulator (SOI) ring resonato. Paper presented at: 2012 Conference on Lasers and Electro-Optics, CLEO 2012, 2012, San Jose.

[46] Cox III CH. Analog optical links: theory and practice. New York: Cambridge University Press, 2006.

[47] Bridges WB, Schaffner JH. Distortion lin linearized electrooptic modulators. IEEE Microw Theory and Techniq 1995;43: 2184–97.

[48] Lee BG, Biberman A, Chan J, Bergmann K. High-performance modulators and switches for silicon photonic networks-on-chip. IEEE J Sel Top Quant 2010;16:6–22.

[49] Khilo A, Sorace C, Kärtner F. Broadband linearized silicon modulator. Opt Exp 2011;19:4485–500.

[50] Yariv A, Koumans R. Time interleaved optical sampling for ultra-high speed A/D conversion. Electron Lett 1998;34:2012–3.

[51] Kang JU, Esman RD. Demonstration of time interweaved photonic four-channel WDM sampler for hybrid analogue-digital converter. Electron Lett 1999;35:60–1.

[52] Juodawlkis PW, Twichell JC, Betts G, Hargreaves JJ. Optically sampled analog-to-digital converters. IEEE T Microw Theory 2001;49:1840–53.

[53] Fang AW, Park H, Jones R, Cohen O, Paniccia MJ, Bowers JE. A Continuous-wave hybrid algainas-silicon evanescent laser. IEEE Photonic Technol Lett 2006;18:1143–5.

[54] Liu J, Kimerling LC, Michel J. Monolithic Ge-on-Si lasers for large-scale electronic-photonic integration. Semicond Sci Technol 2012;27.

[55] Kalman RF, Fan JC, Kazovsky LG. Dynamic range of coherent analog fiber-optic links. J Lightwave Technol 1994;12:1263–77.

[56] Timurdogan E, Biberman A, Trotter DC, Sun C, Moresco M, Stojanovic V, Watts M. Automated wavelength recovery for microring resonators. Paper presented at: 2012 Conference on Lasers and Electro-Optics, CLEO 2012, 2012, San Jose.

[57] Sun J, Timurdogan E, Yaacobi A, Hosseini ES, Watts MR. Large-scale nanophotonic phased array. Nature 2013;493:195–9.